ISSN 1674-1056
http://cpb.iphy.ac.cn
http://iopscience.iop.org/cpb
中国物理 B
Chinese Physics
中国物理 Chinese Physics B

Standing-wave spectrometry in silicon nano-waveguides using reflection-based near-field scanning optical microscopy

Yi-Zhi Sun(孙一之), Wei Ding(丁伟), Bin-Bin Wang(王斌斌), Rafael Salas-Montiel, Sylvain Blaize, Renaud Bachelot, Zhong-Wei Fan(樊仲维), Li-Shuang Feng(冯丽爽)

Citation: Chin. Phys. B . 2019, 28(1): 010702. **doi:** 10.1088/1674-1056/28/1/010702
Journal homepage: http://cpb.iphy.ac.cn; http://iopscience.iop.org/cpb

What follows is a list of articles you may be interested in

Electrically pumped metallic and plasmonic nanolasers

Martin T Hill

Chin. Phys. B . 2018, 27(11): 114210. **doi:** 10.1088/1674-1056/27/11/114210

Two-frequency amplification in a semiconductor tapered amplifier for cold atom experiments

Zhi-Xin Meng(孟至欣), Yu-Hang Li(李宇航), Yan-Ying Feng(冯焱颖)

Chin. Phys. B . 2018, 27(9): 094201. **doi:** 10.1088/1674-1056/27/9/094201

All polymer asymmetric Mach-Zehnder interferometer waveguide sensor by imprinting bonding and laser polishing

Yu Liu(刘豫), Yue Sun(孙月), Yun-Ji Yi(衣云骥), Liang Tian(田亮), Yue Cao(曹悦), Chang-Ming Chen(陈长鸣), Xiao-Qiang Sun(孙小强), Da-Ming Zhang(张大明)

Chin. Phys. B . 2017, 26(12): 124215. **doi:** 10.1088/1674-1056/26/12/124215

unable optical filter using second-order micro-ring resonator

Lin Deng(邓林), Dezhao Li(李德钊), Zilong Liu(刘子龙), Yinghao Meng(孟英昊), Xiaonan Guo(郭小男), Yonghui Tian(田永辉)

Chin. Phys. B . 2017, 26(2): 024209. **doi:** 10.1088/1674-1056/26/2/024209

High-speed and broad optical bandwidth silicon modulator

Xu Hao, Li Xian-Yao, Xiao Xi, Li Zhi-Yong, Yu Yu-De, Yu Jin-Zhong

Chin. Phys. B . 2013, 22(11): 114212. **doi:** 10.1088/1674-1056/22/11/114212

Standing-wave spectrometry in silicon nano-waveguides using reflection-based near-field scanning optical microscopy*

Yi-Zhi Sun(孙一之)[1,2], Wei Ding(丁伟)[2,‡], Bin-Bin Wang(王斌斌)[3], Rafael Salas-Montiel[3], Sylvain Blaize[3], Renaud Bachelot[3], Zhong-Wei Fan(樊仲维)[4], and Li-Shuang Feng(冯丽爽)[1,†]

[1] *School of Instrumentation Science and Opto-Electronics Engineering, Beihang University, Beijing* 100191, *China*
[2] *Laboratory of Optical Physics, Institute of Physics, Chinese Academy of Sciences, Beijing* 100190, *China*
[3] *Laboratoire de Nanotechnologie et d'Instrumentation Optique (LNIO), ICD CNRS UMR* 6281, *Université de Technologie de Troyes, France*
[4] *Academy of Opto-Electronics, Chinese Academy of Science, Beijing* 100094, *China*

(Received 6 November 2018; revised manuscript received 15 November 2018; published online 21 December 2018)

Utilizing reflection-based near-field scanning optical microscopy (NSOM) to image and analyze standing-wave patterns, we present a characterization technique potentially suitable for complex photonic integrated circuits. By raster scanning along the axis of a straight nano-waveguide in tapping mode and sweeping wavelength, detailed information of propagating waves in that waveguide has been extracted from analyses in both space and wavelength domains. Our technique needs no special steps for phase stabilization, thus allowing long-duration and environment-insensitive measurements. As a proof-of-concept test, in a silicon single-mode waveguide with a few of etched holes, the locations and reflection strengths of the inner defects have been quantified. The measurement uncertainty of the reflection amplitude is less than 25% at current stage. Our technique paves the way for non-destructively diagnosing photonic circuits on a chip with sub-wavelength spatial resolution and detailed information extraction.

Keywords: near-field scanning optical microscopes, integrated optics, interferometry

PACS: 07.79.Fc, 42.82.–m, 95.75.Kk **DOI:** 10.1088/1674-1056/28/1/010702

1. Introduction

As lightwave communications and networking continuously stride into ultra-dense large-scale photonic integrated circuits (PICs) in the past decade, the capability of testing circuit parts that are closely spaced becomes increasingly crucial.[1–3] In fiber-optic systems, there are three main diagnostic techniques: optical time domain reflectometry (OTDR), optical low-coherence domain reflectometry (OCDR), and optical frequency domain reflectometry (OFDR).[4–6] OFDR is based on wavelength sweeping of narrow line-width laser in an interferometer. The coherent nature makes this technique superior to the other two in terms of good balance between spatial resolution and detection sensitivity. However, as the complexity of PICs grows,[7] the improvement of the spatial resolution of traditional OFDR, which is inherently restricted by the frequency span of the laser source,[8] cannot catch up with the demand any more.

To solve this problem, other techniques like local light coupling and characterization of evanescent near fields have been resorted to.[9,10] Near-field scanning optical microscopy (NSOM) is a powerful technique with sub-wavelength spatial resolution.[11] Particularly in scattering-type NSOM, a spatial resolution less than 20 nm (two orders of magnitude better than that of traditional OFDR) can be routinely achieved.[12,13]

Meanwhile, inspired by high collection efficiency in so-called transmission-based NSOM,[14,15] we recently proposed and realized a technique referred to as reflection-based NSOM.[16] As illustrated in Fig. 1(a), the interaction of a propagating guided wave with an atomic force microscope (AFM) probe results in conversion of near fields to far-field radiation.[17] In all the radiation directions, the two along the forward and the backward guided modes have very high light collection efficiencies. In other words, these two guided modes can naturally play the role of a high-numerical-aperture lens. In experiment, we arranged an interferometer in the reflection direction and observed greatly enhanced light collection efficiency.[16] Our method, which can be realized in an all-fiber form, eliminates expensive far-field collection systems and overcomes the detrimental effect of background field super-position.[18–20] It can measure both amplitude and phase of optical near field, and the phase drift arising from environmental fluctuations can be self-compensated in a common path interferometer setup.

Having secured advantages in both spatial resolution and detection sensitivity (i.e., light collection efficiency) in Ref. [16], here, we attempt to use reflection-based NSOM in the context of OFDR, which can exploit the wavelength domain, to image standing waves along a silicon nano-waveguide. We develop a theoretical model to decompose the signal beam components based on their different interac-

*Project supported by National Key R&D Program of China (Grant No. 2017YFA0303800), National Natural Science Foundation of China (Grant No. 61575218), and Defense Industrial Technology Development Program, China (Grant No. JCKY201601C006).

†Corresponding author. E-mail: fenglishuang@buaa.edu.cn
‡Corresponding author. E-mail: wding@iphy.ac.cn

© 2019 Chinese Physical Society and IOP Publishing Ltd

tion natures with the AFM probe. The near-field standing-wave profiles are acquired at different wavelengths. Based on Fourier analysis, we explicitly extract useful information about the defects inside the waveguide, including their locations and reflection strengths. Different attributes of light-probe interactions can also be discerned in the near-field mode profiles.

2. Theoretical model

To simplify investigation, we focus on the fundamental quasi-transverse electric (TE) mode, whose major electric field is parallel to the wafer surface, in a straight single-mode silicon-on-insulator (SOI) waveguide. When a silicon AFM probe (NT-MDT, HA_NC) vibrates normal to the top surface of the waveguide at a frequency of $\Omega \approx 250$ kHz, the intensities of the reflected and the transmitted lights are both modulated (see the blue and the red arcs and the black dashed lines in Fig. 1(b)). Note that the blue and the cyan arcs in Fig. 1(b) represent different reflection coefficients in the two directions arising from the geometric asymmetry of the AFM tip. At the front facet of the waveguide, the continuous-wave (CW) light of a tunable laser source (TLS, TUNICS-Plus, with the line-width of 400 kHz) is reflected back to the lensed fiber (see the orange arrow in Fig. 1(b)) and serves as the reference beam in the interferometer. Figure 1(c) shows the experimental setup with an in-line polarization controller (PC) and circulator (Cir) before the device under test (DUT) and an InGaAs detector (Det, Thorlabs, DET10 C/M) and lock-in amplifier (LIA, Zurich Instruments, HF2LI) after the DUT.

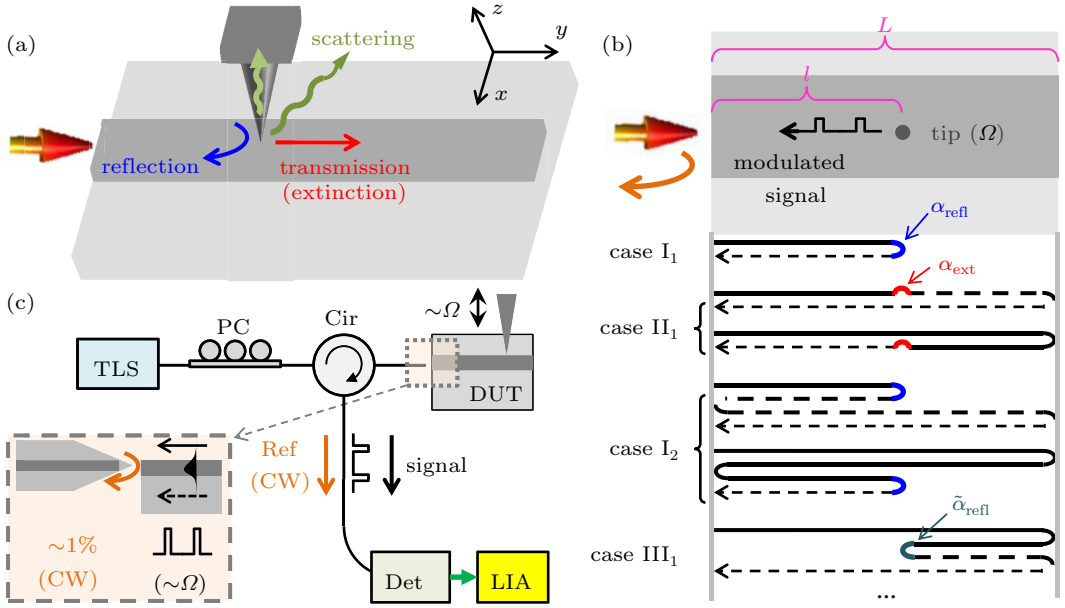


Fig. 1. (a) Schematic of a guided wave being Mie–Rayleigh scattered by an AFM probe. The blue and the red arrows represent the reflection and extinction of light, respectively. (b) Different components of the overall modulated signal beam in the $-y$ direction. The orange arrow represents the CW reference beam. l and L depict the positions of the probe and the back facet, respectively. The dashed lines indicate the light intensity modulations imposed by the vibrated AFM probe. (c) Experimental setup of a reflection-based NSOM. Inset: the light coupled back to the lensed fiber consists of the CW reference beam and the modulated/unmodulated signal beam.

If the reflected light from the rear part of the waveguide cannot be ignored, the total modulated signal beam in the $-y$ direction is comprised of different components. The coordinates (x, y, z) have been depicted in Fig. 1(a). According to the simulation (see section 3), in our situations, when a guided wave interacts with an AFM probe, the amplitude coefficients of the reflection and the extinction are less than 0.005. Therefore, we can neglect all the beam components arising from multiple light–probe interactions. Figure 1(b) schematically illustrates the first three groups of modulated signal beams (case I_m, II_m, and III_m, with m being the number of round-trips). The lock-in demodulated photocurrent from a quadratic detector can be expressed as

$$\eta \approx \sum_{m=1}^{+\infty} \left(\eta_{\mathrm{I}}^{(m)} + \eta_{\mathrm{II}}^{(m)} + \eta_{\mathrm{III}}^{(m)}\right), \tag{1}$$

$$\eta_{\mathrm{I}}^{(m)} \propto 2\left|E_{\mathrm{ref}}\right| \cdot m \left|\alpha_{\mathrm{refl}} E_{\mathrm{I}}^{(m)}\right| \cdot \cos(2\phi_{\mathrm{I}}^{(m)}), \tag{2}$$

$$\begin{aligned}\eta_{\mathrm{II}}^{(m)} &\propto \left|E_{\mathrm{ref}} + E_{\mathrm{II}}^{(m)}\right|^2 - \left|E_{\mathrm{ref}} + E_{\mathrm{II}}^{(m)} - 2m \cdot \alpha_{\mathrm{ext}} E_{\mathrm{II}}^{(m)}\right|^2 \\ &\approx 4m\left|\alpha_{\mathrm{ext}}\right| \left[\left|E_{\mathrm{II}}^{(m)}\right|^2 \cos(\delta_{\mathrm{ext}}) + \left|E_{\mathrm{ref}}\right| \cdot \left|E_{\mathrm{II}}^{(m)}\right| \cos(2\Phi_{\mathrm{II}}^{(m)})\right],\end{aligned} \tag{3}$$

$$\eta_{\mathrm{III}}^{(m)} \propto 2\left|E_{\mathrm{ref}}\right| \cdot m \left|\tilde{\alpha}_{\mathrm{refl}} E_{\mathrm{III}}^{(m)}\right| \cdot \cos(2\phi_{\mathrm{III}}^{(m)}). \tag{4}$$

Here, $E_{\mathrm{ref}}(y)$ and $E_{\mathrm{I,II,III}}^{(m)}(y)$ are the complex electric fields of the reference beam and the signal beams as a function of the y coordinate, respectively. For the signal beams $E_{\mathrm{I,II,III}}^{(m)}$, the in-

/out-coupling losses at the front facet, the propagation losses along the black lines in Fig. 1(b), and the reflection losses at both facets have all been taken into account. Note that, for a single-coupling-point configuration, the in-coupling and out-coupling coefficients are the same. $\alpha_{\rm refl}(x)$ and $\alpha_{\rm ext}(x)$ stand for the complex amplitude coefficients of the reflection and extinction mediated by the AFM probe, respectively. $\alpha_{\rm ext} = |\alpha_{\rm ext}| \cdot \exp(\mathrm{i}\delta_{\rm ext})$. Accordingly, the intensity reflectance and transmittance caused by a single light–probe interaction can be written as $|\alpha_{\rm refl}|^2$ and $|1-\alpha_{\rm ext}|^2$, respectively. For each signal beam component shown in Fig. 1(b), the number of round-trips m determines the number of optional ways in which a propagating wave interacts with the AFM probe at different sequences. Specifically, in cases I_m and III_m, the number of the light–probe interaction is equal to m, and in case II_m, this number becomes $2m$. As an example, figure 1(b) plots the two optional light–probe interaction ways for case II_1. Also, in Eqs. (2)–(4), we neglect all the quadratic terms of the signal fields because $|\alpha \cdot E^{(m)}_{\rm I,II,III}| \ll |E_{\rm ref}|$.

Under such circumstances, in cases I and III, the phase ϕ linearly varies with the probe position l, while in case II, the phase Φ is independent of the probe position,

$$\begin{aligned}
\phi^{(m)}_{\rm I}(l,\lambda) &= [l+(m-1)L]\cdot(2\pi n_{\rm eff}/\lambda)+C_{\rm I},\\
\Phi^{(m)}_{\rm II}(\lambda) &= mL\cdot(2\pi n_{\rm eff}/\lambda)+C_{\rm II},\\
\phi^{(m)}_{\rm III}(l,\lambda) &= [-l+(m+1)L]\cdot(2\pi n_{\rm eff}/\lambda)+C_{\rm III}. \qquad (5)
\end{aligned}$$

Here, λ is the wavelength, $n_{\rm eff}$ is the effective index of the guided mode, and the constant C's stand for the phase differences between α and $E_{\rm ref}$. According to Eqs. (1)–(5), by varying l and λ, we should be able to extract detailed information about the propagating waves.

3. Experiment

3.1. Standing-wave spectrometry

An SOI waveguide with the cross-section of 500 nm × 220 nm is fabricated and satisfies the single-mode condition at $\lambda = 1620$ nm. The calculated effective and group indices of the guided mode are $n_{\rm eff} = 2.30$ and $n_{\rm g} = 4.29$, respectively. The length of the waveguide is $L \approx 4$ mm, and the AFM probe is placed close to the front facet and operates in tapping mode. Figure 2(a) shows the standing-wave profiles acquired by raster scanning the probe along the central axis of the waveguide (see the inset in Fig. 2(b)) at different wavelengths, which is referred to as standing-wave spectrogram (SWS) hereafter. Performing spatial Fourier transform (FT) on the SWS yields two peaks, as shown in Fig. 2(b). The peaks at the zero and non-zero spatial frequencies originate from the contributions of case II (Eq. (3)) and cases I/III (Eqs. (2) and (4)), respectively. The effective wavelength $\lambda_{\rm eff} = 719$ nm derived from the position of the non-zero spatial frequency peak (2.78 $\mu\mathrm{m}^{-1}$) results in $n_{\rm eff} = 2.25$ at $\lambda = 1620.3$ nm, agreeing well with the calculated result of $n_{\rm eff} = 2.30$. With the enlargement of the scanning line and keeping it parallel to the waveguide axis, the accuracy of the measurement of $n_{\rm eff}$ can be greatly improved as indicated in Ref. [21].

Figure 2(c) plots the amplitudes and phases of the two spatial frequency peaks. For the zero spatial frequency peak (case II), the amplitude varies in a sinusoidal fashion with the wavelength spacing $\Delta\lambda \approx 0.08$ nm. From the relationship of $\Delta\lambda = \lambda^2/(2n_{\rm g}L')$, which can describe generic interference process, we estimate $L' \approx 3.8$ mm in good accordance with the total length of the waveguide. This means the back facet of the waveguide produces the main reflection beam. Additionally,

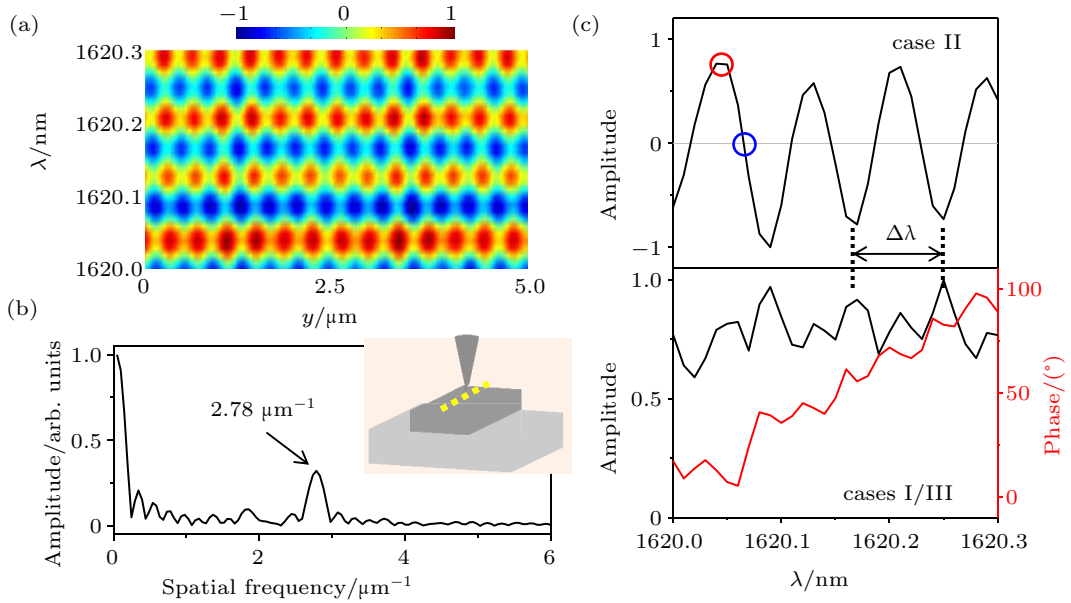


Fig. 2. (a) Standing-wave spectrogram measured along the central axis of the waveguide. (b) Amplitude of the spatial FT of the standing-wave profile acquired at $\lambda = 1620.3$ nm. Insert: an AFM probe repeatedly scans along the yellow dotted line ($x = 0$, z_0). (c) Normalized amplitudes and phases of the zero and non-zero spatial frequency peaks as a function of the wavelength. The red and the blue circles stand for the two wavelengths used in the NSOM imaging (see Fig. 3).

as shown in the top diagram of Fig. 2(c), the second term of Eq. (3) (i.e., the sinusoidally-varying one) is manifest, indicating that the reference beam from the front facet ($E_{\rm ref}$) outweighs the reflected beam from the back facet ($E_{\rm II}$). According to the amplitude spectrum, we can estimate $|E_{\rm II}|/|E_{\rm ref}| < 5\%$. In this circumstance, we only count in case $\rm II_1$, and no phase information can be extracted from the l-independent variable $\eta_{\rm II}^{(1)}$.

With regard to the non-zero spatial frequency peak (cases I/III), as shown in the bottom diagram of Fig. 2(c), the phase spectrum exhibits a quasi-linear variation, and the normalized amplitude spectrum stays in a range of 0.6–1. Considering Eqs. (2), (4), and (5), these two characteristics imply that case $\rm I_1$ plays the dominant role. In order to explain the undulations in these two spectra, we first consider the coherent superposition of $E_{\rm ref}$ and $E_{\rm II}$, which can form a new reference beam in the interferometer and provide a wavelength-dependent amplification gain in the demodulation process. However, the above analysis has verified $|E_{\rm II}| \ll |E_{\rm ref}|$. So, this mechanism should not be sufficient to explain all the undulations. There must be other effects underneath.

From Eq. (2), the overall demodulated signal of case I group can be written as

$$\eta_{\rm I} = \sum \eta_{\rm I}^{(m)} \propto |\alpha_{\rm refl} E_{\rm ref}| \cdot {\rm Re}\Bigg(\sum_{m=1}^{+\infty} m \cdot {\rm e}^{-\gamma l} (R_{\rm round})^{m-1} \times \exp\{{\rm i}2k_{\rm eff}[l + (m-1)L] + {\rm i}2C_{\rm I}\}\Bigg), \tag{6}$$

where $k_{\rm eff} = 2\pi n_{\rm eff}/\lambda$, γ is the intensity attenuation coefficient, $R_{\rm round}$ is the attenuation of one round-trip, and ${\rm Re}(\cdot)$ represents the real part of the expression. In the same way, the overall demodulated signal of case III group is

$$\eta_{\rm III} = \sum \eta_{\rm III}^{(m)} \propto |\tilde{\alpha}_{\rm refl} E_{\rm ref}| \cdot {\rm Re}\Bigg(\sum_{m} m \cdot {\rm e}^{\gamma l} (R_{\rm round})^{m+1} \times \exp\{{\rm i}2k_{\rm eff}[-l + (m+1)L] + {\rm i}2C_{\rm III}\}\Bigg). \tag{7}$$

Summing up Eqs. (6) and (7) yields

$$\eta_{\rm I} + \eta_{\rm III} \propto |E_{\rm ref}| \cdot {\rm Re}\Big[\Big(\alpha_{\rm refl} \cdot {\rm e}^{{\rm i}2C_{\rm I}} X^{-1} + \tilde{\alpha}_{\rm refl} \cdot {\rm e}^{{\rm i}2C_{\rm III}} X\Big) \cdot Y(1-Y)^{-2}\Big], \tag{8}$$

where $X \equiv {\rm e}^{\gamma l} R_{\rm round} \cdot {\rm e}^{{\rm i}2k_{\rm eff}(L-l)}$ and $Y \equiv R_{\rm round} \cdot {\rm e}^{{\rm i}2k_{\rm eff}L}$ with their wavelength spacings $\Delta\lambda_X = \lambda^2/[2n_{\rm g}(L-l)]$ and $\Delta\lambda_Y = \lambda^2/(2n_{\rm g}L) \approx 0.08$ nm, respectively. Taking into account all the components in cases I and III, therefore, the complexity of the resultant spectra in Fig. 2(c) is greatly increased. If $|X| \ll 1$, the contribution of case III can be ignored, and then if $|Y| \ll 1$, equation (8) is degraded to $\left|E_{\rm ref}\alpha_{\rm refl}\,{\rm e}^{-\gamma l}\right| \cdot \cos(2k_{\rm eff}l + 2C_{\rm I})$, which has a constant amplitude and linearly-varying phase.

3.2. Reflection-based NSOM imaging

Near-field imaging has been carried out. At $\lambda = 1620.04$ nm (the red circle in Fig. 2(c)), both the contributions of case II and cases I/III need to be taken into account. We make a line cut in Fig. 3(a) at a y coordinate with $2\phi_{\rm I,III} \approx \pi/2$, where the main contribution of the demodulated signal is from

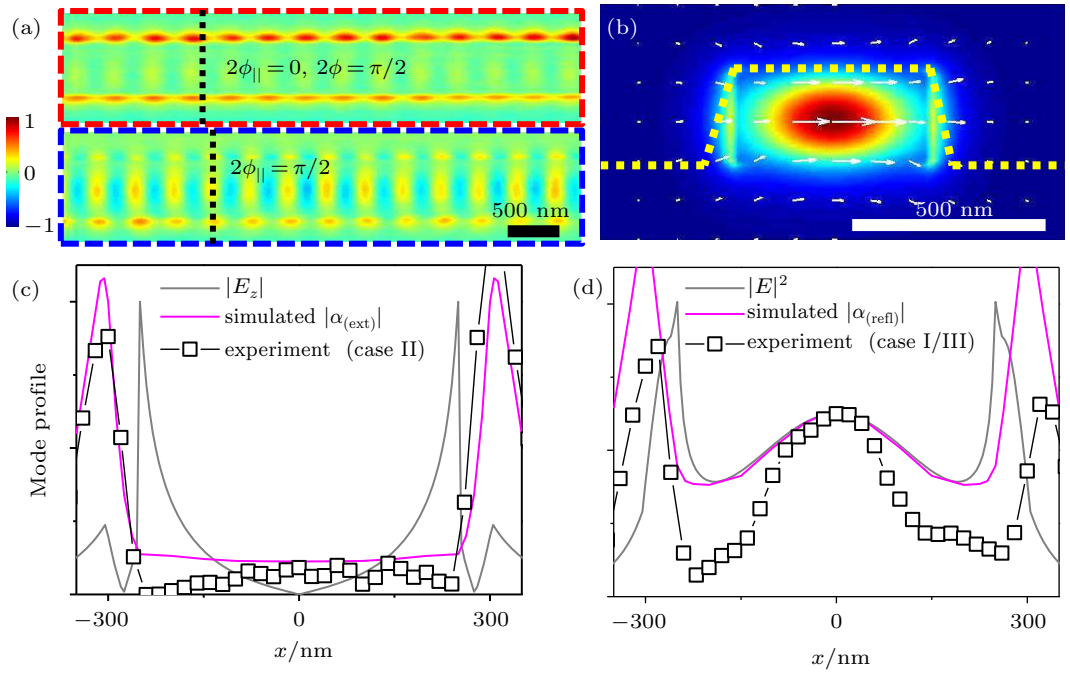


Fig. 3. (a) Near-field images measured by a reflection-based NSOM at $\lambda = 1620.04$ nm and 1620.07 nm, corresponding to $2\Phi_{\rm II} = 0$ and $\pi/2$, respectively. (b) Calculated distributions of the electric field intensity ($|E_x|^2 + |E_y|^2 + |E_z|^2$) and polarization of the guided mode at $\lambda = 1620$ nm. Both scale bars in (a) and (b) are 500 nm. The dotted line in (b) indicates the moving trail of the AFM tip. (c) and (d) Comparisons of the experimental line cuts (hollow squares), the mode profiles (gray lines), and the FDTD simulated $|\alpha_{\rm ext}|$ and $|\alpha_{\rm refl}|$ (magenta lines). Note that the mode profiles $|E_z|$ and $|E|^2$ are just a guide to highlight the effects of different field components.

the extinction interaction. In Fig. 3(c), we compare the experimental result with the calculated mode profile of $|E_z|$ and the simulated $|\alpha_{\text{ext}}|$. The fact that the experimental curve has a low and flat bump in the center and two high and sharp peaks near the edges implies that E_z probably plays the main role. In numerical simulation, a vertical silicon cone with the full cone angle of 30° and the apex radius of 10 nm moves along the dotted line in the transverse plane (see Fig. 3(b)), and a three-dimensional finite-difference time-domain (FDTD) method is employed with the finest mesh size to be 2 nm and the refractive indices of silicon and silica to be 3.475 and 1.444, respectively. Perfectly matched layer (PML) boundaries encircle the simulation space, ensuring a convergence accuracy of $< 0.5\%$.

At another wavelength of $\lambda = 1620.07$ nm (the blue circle in Fig. 2(c)), $2\Phi_{\text{II}} \approx \pi/2$, the contribution of case II is minimized, and the near-field image mainly represents the reflection interaction between the AFM probe and guided waves. In Fig. 3(d), an experimental line cut is compared with the mode profile of $|E|^2$ and the simulated $|\alpha_{\text{refl}}|$. It is seen that the height of the central bump relative to the edge peaks increases remarkably. This means that, except E_z, which is zero in the central region, $E_{x,y}$ also play important roles. Figure 3(b) shows the distributions of the intensity and polarization of the quasi-TE mode in the cross-section at $\lambda = 1620$ nm.

In Figs. 3(c) and 3(d), the ratios of the heights of the central bump and the edge peaks are generally consistent between experiment and simulation. The discrepancy may be ascribed to the non-ideal shape and tilting angle of the tip. Very interestingly, the results of Fig. 3 imply that when we consider a dielectric conical probe and a highly confined quasi-TE mode, the extinction coefficient α_{ext} can be approximately treated as a convolution of E_z, while the reflection coefficient α_{refl} needs to include all the three electric field components.

3.3. Detecting defects in a waveguide

Employing the model established above, we investigate another waveguide with etched holes in the middle. Figure 4(a) depicts the waveguide length $L = L_1 + L_2$ and the position of the holes $L_1 \approx 0.6L$. Figure 4(b) shows the scanning electron microscope (SEM) image. Around the wavelength of 1620 nm, the reflectance and transmittance of these holes can be regarded as constants. When the AFM probe is placed between the front facet and the holes (position A), the middle

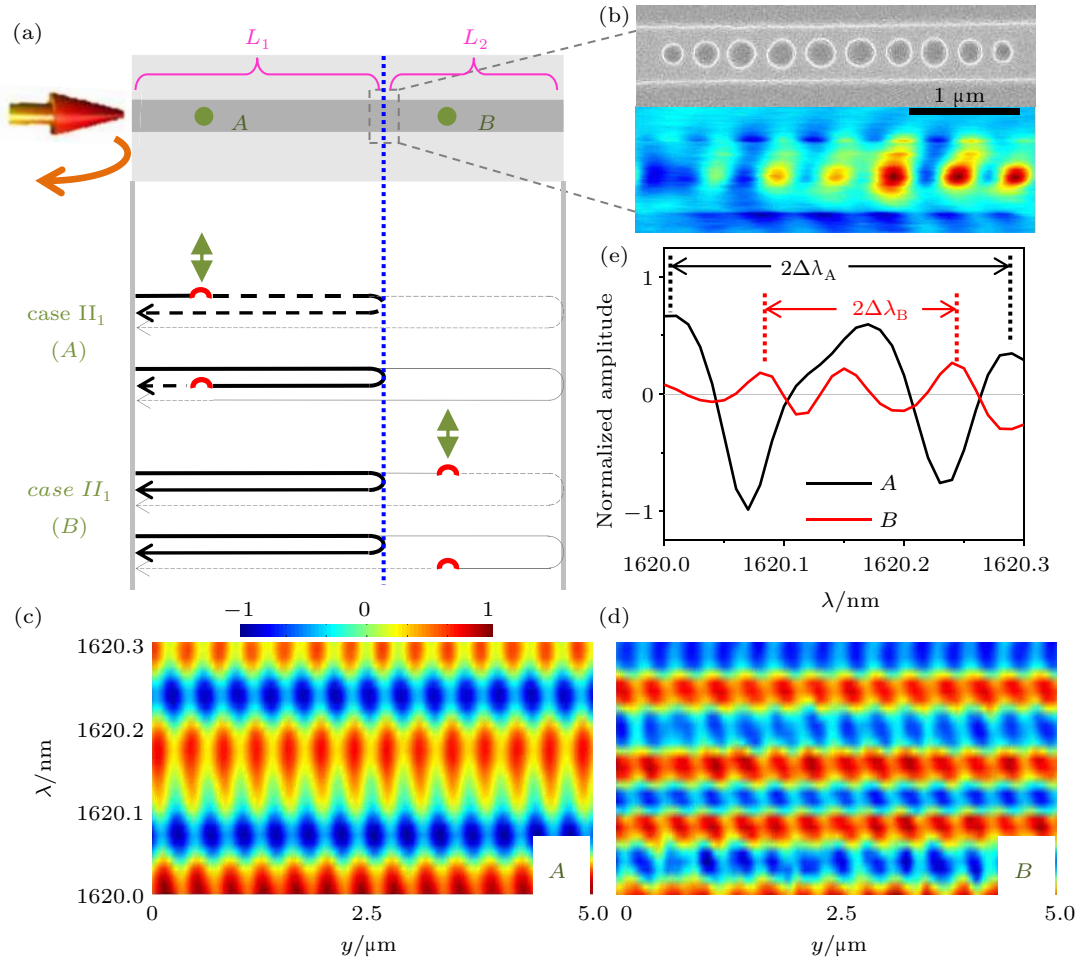


Fig. 4. (a) Schematic of light–probe interactions in a waveguide with etched holes. The length of the waveguide $L = L_1 + L_2 \approx 4$ mm, and the etched holes are located at $L_1 \approx 0.6L$. When the AFM probe is vibrated at position A or B, the component signal beams of case II$_1$ are depicted. (b) SEM image of the etched holes and near-field image measured by the reflection-based NSOM at $\lambda = 1620$ nm. (c) and (d) SWS acquired at positions A and B. (e) Amplitude spectra of the zero-spatial-frequency components of the SWS in (c) and (d).

portion of Fig. 4(a) depicts the two beam components of case II_1. We hypothesize that $|E_{\mathrm{ref}}| > |E_{\mathrm{refl}}^{(\mathrm{def})}| > |E_{\mathrm{refl}}^{(\mathrm{back})}|$ with $E_{\mathrm{refl}}^{(\mathrm{def})}$ and $E_{\mathrm{refl}}^{(\mathrm{back})}$ being the lights reflected by the holes and the back facet, respectively. Equation (3) becomes

$$\begin{aligned}\eta_{\mathrm{II}}^{(1)} \propto & \left|E_{\mathrm{ref}}+E_{\mathrm{refl}}^{(\mathrm{def})}+E_{\mathrm{refl}}^{(\mathrm{back})}\right|^2-\left|E_{\mathrm{ref}}+E_{\mathrm{refl}}^{(\mathrm{def})}+E_{\mathrm{refl}}^{(\mathrm{back})}\right. \\ & \left.-2\alpha_{\mathrm{ext}}E_{\mathrm{refl}}^{(\mathrm{def})}-2\alpha_{\mathrm{ext}}E_{\mathrm{refl}}^{(\mathrm{back})}\right|^2 \\ \approx & \, 4|\alpha_{\mathrm{ext}}|\left[\left|E_{\mathrm{refl}}^{(\mathrm{def})}\right|^2\cos(\delta_{\mathrm{ext}})+|E_{\mathrm{ref}}|\cdot\left|E_{\mathrm{refl}}^{(\mathrm{def})}\right|\cos\left(2\Phi_{\mathrm{refl}}^{(\mathrm{def})}\right)\right. \\ & \left.+|E_{\mathrm{ref}}|\cdot\left|E_{\mathrm{refl}}^{(\mathrm{back})}\right|\cos\left(2\Phi_{\mathrm{refl}}^{(\mathrm{back})}\right)\right], \end{aligned} \tag{9}$$

where $\Phi_{\mathrm{refl}}^{(\mathrm{def})}(\lambda)=L_1\cdot(2\pi n_{\mathrm{eff}}/\lambda)+C_{\mathrm{II}}$, $\Phi_{\mathrm{refl}}^{(\mathrm{back})}(\lambda)=L\cdot(2\pi n_{\mathrm{eff}}/\lambda)+C_{\mathrm{II}}$, and the other higher-order terms are neglected. The SWS acquired in reflection-based NSOM is shown in Fig. 4(c). The amplitude at the zero spatial frequency is plotted in Fig. 4(e) as a black spectrum and is mainly governed by the first two terms in Eq. (9). According to the relationship of $\Delta\lambda_A=\lambda^2/(2n_{\mathrm{g}}L_1)$, the wavelength spacing $\Delta\lambda_A\approx 0.14$ nm is in good agreement with the measured distance between the front facet and the holes. The downshift of the black spectrum relative to zero is caused by the first term in Eq. (9) and can help us to estimate $|E_{\mathrm{refl}}^{(\mathrm{def})}|/|E_{\mathrm{ref}}|\approx 1/5$. Additionally, the last term in Eq. (9) has a wavelength spacing of $\lambda^2/(2n_{\mathrm{g}}L)$ and can be discriminated in the FT trace of the black spectrum as a third peak. Comparing all the peaks in the FT trace yields $|E_{\mathrm{refl}}^{(\mathrm{back})}|/|E_{\mathrm{refl}}^{(\mathrm{def})}|\approx 1/1.9$.

When the AFM probe moves to position B, the lower portion of Fig. 4(a) depicts the two beam components of case II_1. The demodulated signal becomes

$$\begin{aligned}\eta_{\mathrm{II}}^{(1)} \propto & \left|E_{\mathrm{ref}}+E_{\mathrm{refl}}^{(\mathrm{def})}+E_{\mathrm{refl}}^{(\mathrm{back})}\right|^2 \\ & -\left|E_{\mathrm{ref}}+E_{\mathrm{refl}}^{(\mathrm{def})}+E_{\mathrm{refl}}^{(\mathrm{back})}-2\alpha_{\mathrm{ext}}E_{\mathrm{refl}}^{(\mathrm{back})}\right|^2 \\ \approx & \, 4|\alpha_{\mathrm{ext}}|\left[\left|E_{\mathrm{refl}}^{(\mathrm{back})}\right|^2\cos(\delta_{\mathrm{ext}})+|E_{\mathrm{ref}}|\cdot\left|E_{\mathrm{refl}}^{(\mathrm{back})}\right|\cos\left(2\Phi_{\mathrm{refl}}^{(\mathrm{back})}\right)\right. \\ & \left.+\left|E_{\mathrm{refl}}^{(\mathrm{def})}\right|\cdot\left|E_{\mathrm{refl}}^{(\mathrm{back})}\right|\cos\left(2\Phi_{\mathrm{refl}}^{(\mathrm{def\text{-}back})}\right)\right], \end{aligned} \tag{10}$$

where $\Phi_{\mathrm{refl}}^{(\mathrm{back})}(\lambda)=L\cdot(2\pi n_{\mathrm{eff}}/\lambda)+C_{\mathrm{II}}$, $\Phi_{\mathrm{refl}}^{(\mathrm{def\text{-}back})}(\lambda)=L_2\cdot(2\pi n_{\mathrm{eff}}/\lambda)$, and $L_2=L-L_1$. Figure 4(d) shows the acquired SWS with the amplitude at the zero spatial frequency being plotted in Fig. 4(e) as a red spectrum. The main feature of the red spectrum is determined by the second term in Eq. (10) with the wavelength spacing $\Delta\lambda_B\approx 0.08$ nm, in accordance with $L\approx 4$ mm. In comparison with Eq. (9), the first term of Eq. (10) becomes even smaller because $|E_{\mathrm{refl}}^{(\mathrm{back})}|<|E_{\mathrm{refl}}^{(\mathrm{def})}|$. Accordingly, the vertical shift of the red spectrum relative to zero becomes nearly indiscernible. Additionally, performing FT on the red spectrum can help us to analyze the third term in Eq. (10), whose wavelength spacing is $\lambda^2/(2n_{\mathrm{g}}L_2)$. In this manner, the estimated results of $|E_{\mathrm{refl}}^{(\mathrm{def})}|/|E_{\mathrm{ref}}|\approx 1/4.7$ and $|E_{\mathrm{refl}}^{(\mathrm{back})}|/|E_{\mathrm{refl}}^{(\mathrm{def})}|\approx 1/2.4$ agree well with the results derived from the black spectrum (i.e., the measurement at position A) within a deviation less than 25%.

Thanks to the spatial degree of freedom provided by the AFM probe, our method exhibits a unique feature that measurements at different places can be cross-checked. This is totally different from "black-box-type" techniques. The above experiments are only implemented at two places with the analysis to the demodulated signal at zero spatial frequency. With the increase of the number of testing places and the expansion of the wavelength sweeping range, more accurate measurement should be possible. Furthermore, once the number of defects in a waveguide or a PIC increases, a flexible light launching approach, like a grating attached on a fiber facet (see Ref. [9]), may be needed. Under that circumstance, the single-coupling-point configuration adopted in our method will be more convenient than the two-coupling-point scenario suggested in Ref. [9].

4. Conclusion and perspectives

In summary, utilizing phase-resolved reflection-based NSOM and performing spatial/wavelength FT on standing-wave spectrogram, we combine high spatial resolution, high collection efficiency, and detailed information extraction in the diagnosis of a silicon nano-waveguide. Different from "black-box-type" measurement, our method introduces a small probe into any place along a waveguide so that it has potential to characterize more complex nano-photonic structures.[22,23] In the context of homodyne detection, the reflection/extinction interactions between the AFM probe and the guided waves, both taking place in the local near field, can be discriminated at different spatial frequencies. These two light–probe interactions can also be discerned in the transverse mode profiles at different wavelengths. In contrast, scattering-based NSOM is only relevant to one light–probe interaction,[20] and in transmission-based NSOM, different natures of these two light–probe interactions have not been explicitly identified to the best of our knowledge.[24]

In terms of quantifying locations and reflection strengths of the inner defects in a nano-waveguide, our method obtains advantages of high spatial resolution from NSOM and coherent nature owing to the narrow line-width of the laser source. We develop a theoretical model to decompose the modulated signal beam and preliminarily test its validity. In the future development, both the space and wavelength domains can be further exploited.

References

[1] Agrell E, Karlsson M, Chraplyvy A, Richardson D J, Krummrich P M, Winzer P, Roberts K, Fischer J K, Savory S J, Eggleton B J, Secondini

M, Kschischang F R, Lord A, Prat J, Tomkos I, Bowers J E, Srinivasan S, Brandt-Pearce M and Gisin N 2016 *J. Opt.* **18** 063002
[2] Kopp C, Bernabé S, Bakir B B, Fedeli J, Orobtchouk R, Schrank F, Porte H, Zimmermann L and Tekin T 2011 *IEEE J. Sel. Top. Quantum Electron.* **17** 498
[3] Streshinsky M, Ding R, Liu Y, Novack A, Galland, C, Lim A J, Lo P G, Baehr-Jones T and Hochberg M 2013 *Opt. Photonics News* **24** 32
[4] Eickhoff W and Ulrich R 1981 *Appl. Phys. Lett.* **39** 693
[5] Soller B J, Gifford D K, Wolfe M S and Froggatt M E 2005 *Opt. Express* **13** 666
[6] Zhao D, Pustakhod D, Williams K and Leijtens X 2017 *IEEE Photon. Technol. Lett.* **29** 1379
[7] Heck M J R, Bauters J F, Davenport M L, Doylend J K, Jain S, Kurczveil G, Srinivasan S, Tang Y and Bowers J E 2013 *IEEE J. Sel. Top. Quantum Electron.* **19** 6100117
[8] Glombitza U and Brinkmeyer E 1993 *J. Lightw. Technol.* **11** 1377
[9] Scheerlinck S, Taillaert D, van Thourhout D and Baets R 2008 *Appl. Phys. Lett.* **92** 031104
[10] Rotenberg N and Kuipers L 2014 *Nat. Photon.* **8** 919
[11] Pohl D W, Denk W and Lanz M 1984 *Appl. Phys. Lett.* **44** 651
[12] Bachelot R, Gleyzes P and Boccara A C 1995 *Opt. Lett.* **20** 1924
[13] Inouye Y and Kawata S 1994 *Opt. Lett.* **19** 159
[14] Hopman W C L, van der Werf K O, Hollink A J, Bogaerts W, Subramaniam V and de Ridder R M 2006 *Opt. Express* **14** 8745
[15] Robinson J T, Preble S F and Lipson M 2006 *Opt. Express* **14** 10588
[16] Sun Y Z , Wang B B , Salas-Montiel R, Blaize S, Bachelot R, Feng L S and Ding W 2018 *Opt. Lett.* **43** 4863
[17] Bohren C and Huffman D 1983 *Absorption and Scattering of Light by Small Particles* (New York: John Wiley & Sons)
[18] Stefanon I, Blaize S, Bruyant A, Aubert S, Lerondel G, Bachelot R and Royer P 2005 *Opt. Express* **13** 5553
[19] Ocelic N, Huber A, and Hillenbr R 2006 *Appl. Phys. Lett.* **89** 101124
[20] Bruyant A, Lerondel G, Blaize S, Stefanon I, Aubert S, Bachelot R and Royer P 2006 *Phys. Rev. B* **74** 075414
[21] Lerondel G, Sinno A, Chassagne L, Blaize S, Ruaux P, Bruyant A, Topcu S, Royer P and Alayli Y 2009 *J. Appl. Phys.* **106** 044913
[22] Luo Y, Chamanzar M, Apuzzo A, Salas-Montiel R, Nguyen K N, Blaize S and Adibi A 2015 *Nano Lett.* **15** 849
[23] Sun Y Z, Feng L S, Bachelot R, Blaize S and Ding W 2017 *Opt. Express* **25** 17417
[24] Robinson J T and Lipson M 2011 *Opt. Express* **19** 18380